ACS SENSORS

pubs.acs.org/acssensors Article

Boosting Room Temperature Sensing Performances by Atomically Dispersed Pd Stabilized via Surface Coordination

Xiao-Liang Ye, Shu-Juan Lin, Jiang-Wei Zhang,* Hui-Jie Jiang, Lin-An Cao, Ying-Yi Wen, Ming-Shui Yao, Wen-Hua Li, Guan-E Wang, and Gang Xu*

Cite This: *ACS Sens.* 2021, 6, 1103−1110 Read Online

ACCESS | Metrics & More | Article Recommendations | Supporting Information

ABSTRACT: The urgent requirement of monitoring air pollution worldwide evokes intensive research interest in developing chemiresistive gas sensing techniques. To overcome the limits in sensitivity and selectivity of room temperature (RT) chemiresistive sensing materials, a new strategy using single-atom catalysts (SACs) via surface coordination is proposed. As a proof-of-concept, single Pd atoms on TiO_2 (Pd_1-TiO_2) possess high efficiency in generating adsorbed O_2^- as well as high activity and selectivity in catalyzing CO oxidation at RT. As a result, Pd_1-TiO_2 shows record high sensitivity among the reported RT sensing materials, which is even comparable to those of the best materials working at high temperature. It also provides an approximately 1 order of magnitude lower limit of detection than the best CO sensing materials. Moreover, Pd_1-TiO_2 presents high selectivity toward 12 kinds of interference gases. This work not only paves a way to design high-performance RT gas sensing materials but also extends the application of SACs.

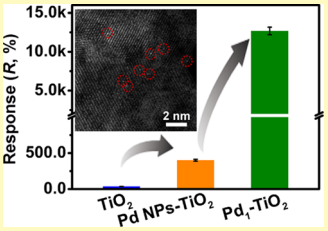

KEYWORDS: *single-atom catalysts, metal oxide, chemiresistive sensing material, carbon monoxide detection, surface coordination*

With the rapid development of industrialization and urbanization, people are facing severe environmental issues worldwide. For example, air pollution is estimated to lead to the death of 7 million people annually (from the World Health Organization, WHO)[1] and will cost the world a massive $2.6 trillion per year by 2060 (from the Organization for Economic Cooperation and Development, OECD).[2] Carbon monoxide (CO), nitrogen oxides (NO_x), and sulfur oxide (SO_x) are the main gas pollutants that require close monitoring.[3] Commercial techniques, such as mass spectrometry[4] and gas chromatography,[5] have been developed for identification and quantitative analysis of these gas pollutants. However, these techniques are non-real-time sensing techniques, which normally require long analysis time, complicated sample preparation, costly instruments, and professional operators. It is desirable to realize fast and real-time gas sensing with high sensitivity and selectivity in building Internet of Things (IoT) for environmental monitoring, yet extremely challenging.

Chemiresistive sensors are a type of real-time detection technique with advantages of high sensitivity, fast response, easy operation, and low production cost.[6,7] They are attracting more and more research interest, while still limited by low sensitivity at room temperature (RT) and poor selectivity in practical applications.[8,9] The representative sensing materials, metal oxides (MOs), require high working temperature (normally >250 °C) to promote the generation of active oxygen species (O_2^-, O^-, and O^{2-}) for the sensing reaction.[10] However, at high temperature, these oxygen species are highly active and can indiscriminately react with the adsorbed gaseous analytes, resulting in the poor selectivity of MOs. Moreover, high working temperature not only increases the ignition risk when detecting flammable gases but also complicates the device fabrication and increases the energy consumption. Loading with a catalytically active metal nanoparticle (NP) catalyst is one of the most used methods to improve the performances for RT sensing.[8,11,12] However, metal NPs usually have relatively low catalytic activity at ambient conditions. Meanwhile, many factors, such as different crystal facets of metal NPs,[13] synergetic effect from neighboring metal atoms,[14] and inhomogeneous distribution of different metal atoms in alloy NPs,[15,16] would result in multiple catalytically active sites, which can simultaneously activate various analytes and degrade their selectivity. At present, the sensitivity and selectivity of metal NP catalyst-loaded MOs at RT are still unsatisfactory.

Single-atom catalysts (SACs),[17−19] which possess both high catalytic activity and selectivity, have drawn tremendous interest in various catalyst-related applications, including energy and organic conversions.[20−23] Superior to the NP catalysts for the heterogeneous catalysis, SACs can achieve much higher catalytic efficiency due to their almost 100% atomic utilization.[19] Moreover, surface-coordinated SACs have

Received: November 12, 2020
Accepted: February 1, 2021
Published: February 12, 2021

https://dx.doi.org/10.1021/acssensors.0c02369
ACS Sens. 2021, 6, 1103−1110

pure, isolated, and structure-identifiable catalytic active sites in statistics.[19,24] Thus, the catalytic selectivity of SACs to different reactants can be flexibly regulated through the selection of metal atoms,[25−28] substitution of supporting substrates,[29−32] modulation of the metal atoms' coordination environment.[17,33−35] Therefore, surface-coordinated SAC-based MOs are very promising to meet the requirements of RT sensing material in both high sensitivity and selectivity. Unfortunately, the research works on SAC-based gas sensing materials are in their infancy stage and the previous works still require additional heating, which complicates the device fabrication.[36−40]

In this work, TiO_2 was selected as a semiconductor material for gas sensing. The nanoflower morphology of TiO_2 enabled it to have a large specific surface area for supporting Pd single atoms. A Pd SAC coordinated on the surface of TiO_2 nanoflowers (denoted as Pd_1-TiO_2)[24] was rationally designed to demonstrate the high performances of SAC-based gas sensing materials at RT. As a relative prototype example, CO was selected as the analyte because it not only is related to outdoor air pollution and household living security but also should be monitored to avoid catalyst poison in the chemical industry and fuel cells.[25,41] Gas sensing tests revealed that compared with Pd nanoparticles, single Pd atoms exhibit much higher efficiency in prompting the sensing performances of TiO_2 nanoflowers. The efficient interface of Pd−O−Ti was constructed by surface coordination between Pd atoms and TiO_2 to enhance the catalytic oxidation of CO at RT. Pd_1-TiO_2 showed unprecedentedly high sensitivity in CO detection, which is superior over all of the reported sensing materials working at RT. The high response endowed it with 1 order of magnitude lower limit of detection (LOD) than the best materials. Pd_1-TiO_2 also presented unique selectivity between CO and other 12 commonly existing interference gases. The possible mechanism for the high sensitivity and selectivity of Pd_1-TiO_2 was also revealed by X-ray photoelectron spectroscopy (XPS), diffuse reflectance infrared Fourier transform (DRIFT) spectroscopy, and theoretical density functional theory (DFT) calculations. Notably, this work represents the first research of SAC-based gas sensing materials capable of working at RT.

EXPERIMENTAL SECTION

Chemicals. Palladium chloride ($PdCl_2$, 98%) was purchased from Sigma-Aldrich. Titanium(III) trichloride (15.0−20.0% $TiCl_3$ basis in 30% HCl) and ethylene glycol (EG) were purchased from Alfa Aesar. Hydrochloric acid (HCl ∼ 35%) and ethanol were purchased from Xinweicheng Co., Ltd., (Fuzhou, China). Unless otherwise noted, materials obtained from commercial suppliers were used without further purification. All aqueous solutions were prepared with Milli-Q water (18.2 MΩ). Ag−Pd interdigital electrode plates with a channel of 200 μm were obtained from Hangzhou Jinbo Tech. Co., Ltd., China. The electrode plates were rinsed with water and dried with nitrogen before use.

Preparation of TiO_2 Nanoflowers. TiO_2 nanoflowers were prepared according to the reported literature with a modified synthetic method.[24,42] Briefly, $TiCl_3$ (1 mL) and EG (20 mL) were mixed and stirred for 10 min before adding 1 mL of water. The light yellow homogeneous solution was allowed to react at 160 °C for 6 h in a Teflon-lined stainless steel autoclave before it was cooled to room temperature in 12 h. A white product was obtained via centrifugation at the speed of 8000 rpm for 5 min, which was further washed with water and ethanol. After drying in a vacuum oven, TiO_2 nanoflowers were collected for characterization and further experiments.

Preparation of Pd_1-TiO_2 Nanoflowers. Pd_1-TiO_2 nanoflowers were prepared by a simple and mild photochemical method at RT according to the previous report.[24] First, 17.4 mg of TiO_2 nanoflowers were dispersed in 10 mL of water before adding a H_2PdCl_4 solution (0.845 mL, 5 mmol L^{-1}) under stirring. The mixture was then exposed to UV light under stirring. The UV treatment was conducted on an LED light source system (Beijing Perfectlight Technology Co., Ltd., PLS-LED 100) with an optical filter that only allows the transmission of 365 nm UV. The power density of the UV light was measured to be about 10 mW cm^{-2} by a radiometer (Beijing Perfectlight Technology Co., Ltd., PL-MW 2000). After UV irradiation for 5 min, a light gray product was obtained by centrifugation, which was further washed by water. The Pd_1-TiO_2 nanoflowers were dried in a vacuum oven and collected for the next test. For comparison, TiO_2 nanoflowers with Pd NP loading were synthesized with a similar method with 30 min UV irradiation and labeled as Pd NPs-TiO_2. For each sample, such as TiO_2, Pd NPs-TiO_2, and Pd_1-TiO_2, more than three batches were prepared individually following the above constant synthesis process.

Characterization. The nitrogen adsorption/desorption measurements were performed using a Micromeritics ASAP2020 gas-sorption system. The sample was first degassed at 100 °C for 8 h before measurements. Thermogravimetric analysis (TGA) experiments were conducted on an STA449C under an air atmosphere with a heating rate of 10 °C min^{-1}. Powder X-ray diffraction (PXRD) was conducted on a Rigaku Smartlab X-ray diffractometer with Cu Kα1 radiation (λ = 1.5406 Å) at a scanning speed of 10° min^{-1}. Morphology details were examined using field emission scanning electron microscopy (FE-SEM, JEOL JSM-6700F) and transmission electron microscopy (TEM, Tecnai F20). High-angle annular dark-field scanning transmission electron microscopy (HAADF-STEM) images were collected on a JEOL JEM-2100F. Aberration-corrected HAADF-STEM images were acquired on a JEOL JEM-ARM200F equipped with a CEOS probe corrector. Samples for TEM were dispersed in ethanol by ultrasonication, and the resulting solution was dropped onto carbon films supported on copper grids. X-ray absorption fine structure spectra (Pd K-edge) were recorded at the XAS station (BL14W1) of the Shanghai Synchrotron Radiation Facility (SSRF), China at 3.5 GeV with a maximum current of 300 mA. Hard X-ray was monochromatized with a Si(111) double-crystal monochromator. The data were collected in the fluorescence mode, while the corresponding reference samples were collected in the transmission mode using a Lytle detector. The sample was ground and uniformly daubed on a special adhesive tape (see details in the Supporting Information (SI)). The data of X-ray photoelectron spectroscopy (XPS) and ultraviolet photoelectron spectroscopy (UPS) were collected from a Thermo Scientific ESCALAB 250 Xi XPS system (monochromatic Al Kα X-rays (1486.6 eV) operating at 15 kV; the base pressure: 5.0×10^{-8} Pa). The samples were first dried in a vacuum oven for 8 h before XPS and UPS tests. The spectra data were analyzed using XPS-Peak software. The ultraviolet−visible (UV−vis) absorption spectra in the diffuse reflection mode were recorded on a PerkinElmer Lambda-900 UV−vis spectrophotometer. In situ diffuse reflectance infrared Fourier transform (DRIFT) spectroscopy experiments were performed on a 6700 Fourier transform infrared spectrometer (Nicolet) equipped with a stainless steel in situ IR flow cell and set up for diffuse reflectance sampling. X-band electron spin resonance ESR spectra were recorded by a Bruker-BioSpin microspectrometer at 90 K. All of the measurements were carried out in the absence of UV light. Fifty milligrams of the samples were placed into NMR tubes and cooled to 90 K by the use of a liquid nitrogen stream for measurements.

Gas Sensing Measurement. The gas sensors were fabricated by a traditional drop-coating method. The prepared sample of Pd_1-TiO_2 nanoflowers was dispersed in ethanol. Subsequently, the dispersion containing 1.0 mg of the sample was drop-coated on the Ag−Pd interdigital electrode. The obtained Pd_1-TiO_2 sensors were aged at 80 °C for 8 h before the test. Meanwhile, TiO_2 gas sensors and Pd NPs-TiO_2 gas sensors were fabricated with a similar method and tested under the same conditions. These mentioned sensors above were

https://dx.doi.org/10.1021/acssensors.0c02369
ACS Sens. 2021, 6, 1103−1110

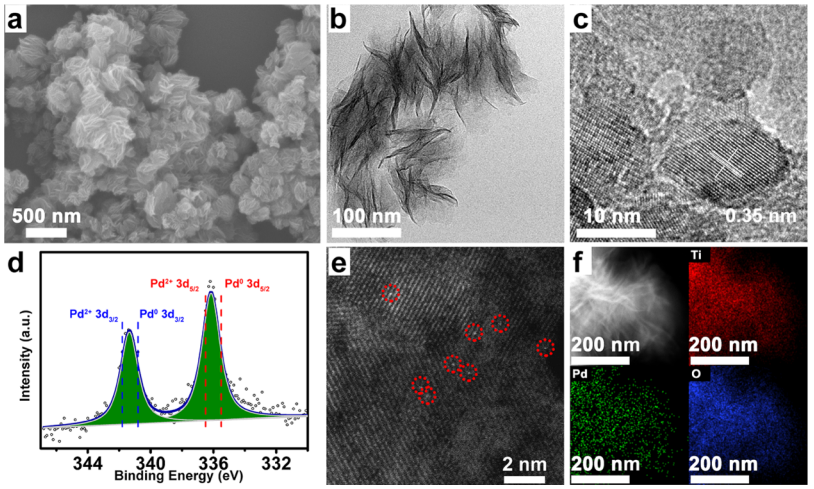

Figure 1. Pd_1-TiO_2 characterization. (a–c) SEM and TEM images, (d) deconvoluted narrow scan Pd 3d XPS spectrum, (e) ac-HAADF-STEM image, and (f) STEM-EDS elemental mapping images.

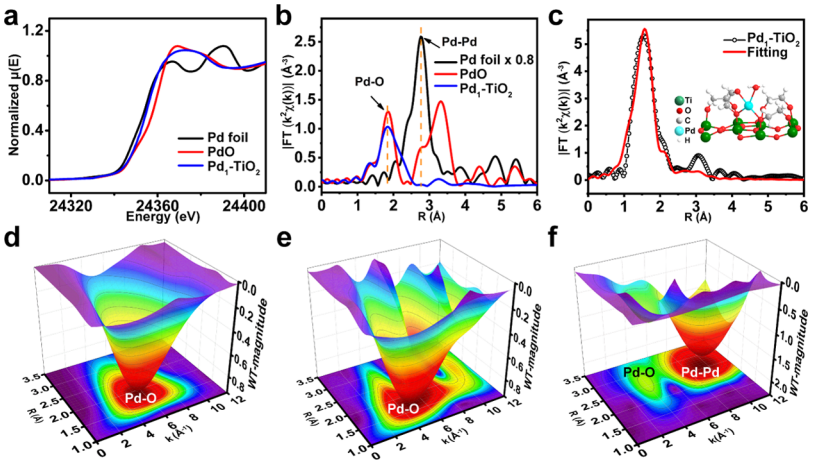

Figure 2. X-ray absorption analysis. (a) XANES and (b) k^2-weighted FT-EXAFS spectra at the Pd K-edge of Pd_1-TiO_2, PdO, and Pd foil. (c) The corresponding fit of the EXAFS spectrum of Pd_1-TiO_2 at the R space. The inset shows the local structure of the Pd_1 species on TiO_2. The WT of the experimental EXAFS spectra of (d) Pd_1-TiO_2, (e) PdO, and (f) Pd foil.

fabricated and tested using samples from different batches. The sensor testing performances were evaluated by a homemade system reported in our early work.[43] The constant gas flow was 600 mL min^{-1}, the bias on the sensor was set to be 5 V (if not specified) and the current data were recorded using a Keithley 2602B sourcemeter. Gases with accurate concentration were generated by mixing target gases with dry air in a certain ratio via mass flow controllers (CS-200C, Beijing Sevenstar Qualiflow Electronic Equipment Manufacturing Co., Ltd., China) and then injected into a quartz tube. The coefficient of variation (CV) was estimated by $R_{SD}/R_{avg} \times 100\%$, where R_{SD} and $R_{avg.}$ are the standard deviation (SD) and the average value of responses, respectively.

RESULTS AND DISCUSSION

Structural and Morphological Characterization of the Samples. TiO_2 nanoflowers (a BET surface area of 326.9 m^2 g^{-1}, Figure S1a) used as the support for Pd atoms were prepared (see experimental details above). Surface coordinated EG (21.6 wt % from TGA, Figure S1b) on TiO_2 ensured the stabilization of Pd SACs. The powder X-ray diffraction (PXRD) pattern (Figure S2) shows that these TiO_2 nanoflowers are a metastable phase of TiO_2(B). Pd_1-TiO_2 was prepared by a reported photochemical method via surface coordination at RT.[24] For comparison, TiO_2 nanoflowers loaded with Pd NPs (Pd NPs-TiO_2) were synthesized by elongating light irradiation.

Scanning electron microscopy (SEM) measurements of TiO_2, Pd NPs- or Pd_1-TiO_2, show the similar nanoflower morphology (Figures 1a, S3, and S4). No Pd NPs were found in pure TiO_2 (Figure S5) and Pd_1-TiO_2 (Figure 1b,c) from transmission electron microscopy (TEM) images. An interplanar spacing of 0.35 nm belonged to (110) of TiO_2 (Figures 1c and S6). In contrast, Pd particles of 5 nm with different contrasts to TiO_2 could be found in Pd NPs-TiO_2 (Figure S6). These particles show lattice fringes of 0.221 nm, which belong to the d_{111} spacing of Pd NPs (Figure S6b).

The aberration-corrected high-angle annular dark-field STEM (HAADF-STEM) image depicted that ultrasmall bright spots were uniformly dispersed on TiO_2 nanoflowers (Figure 1e), suggesting that Pd species existed in the form of isolated single atoms. STEM-EDS elemental mapping diagrams of Pd_1-TiO_2 (Figure 1f) illustrated that Ti, O, and Pd elements were well distributed throughout the nanoflowers. In XPS, the Pd 3d spectrum of Pd_1-TiO_2 exhibited two major signals ($3d_{5/2}$ and $3d_{3/2}$) located at 336.2 and 341.4 eV, respectively, which were between those of Pd^{2+} and Pd^0, indicating the partial oxidation state of anchored Pd atoms (Figures 1d and S7b).[44]

https://dx.doi.org/10.1021/acssensors.0c02369
ACS Sens. 2021, 6, 1103–1110

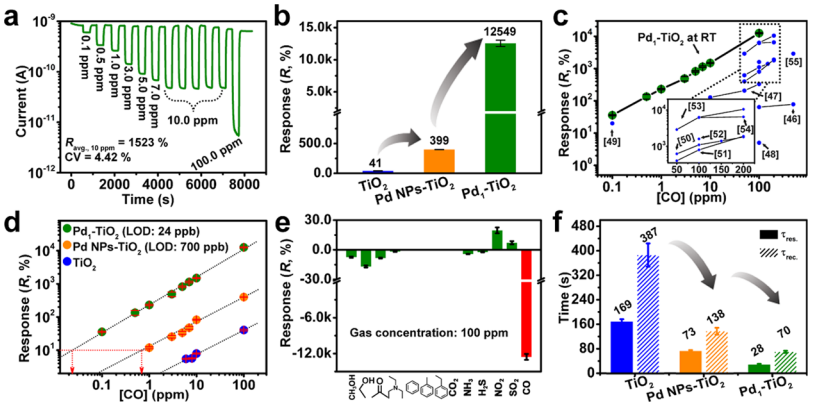

Figure 3. RT gas sensing performances of Pd_1-TiO_2. (a) Typical response−recovery curve of the Pd_1-TiO_2 sensor to CO with different concentrations (0.1−100 ppm). (b) Column charts of responses to 100 ppm CO of pristine TiO_2, Pd NPs-TiO_2, and Pd_1-TiO_2 nanoflowers. (c) Responses of Pd_1-TiO_2 sensors as a function of CO concentration in comparison with those of representative reported RT CO sensors previously (Ti^{3+}-TiO_2,[49] NiO-TiO_2,[50] Pd NPs-TiO_2-rGO,[51] Pd/ZnO,[52] Pd-In_2O_3,[53] Au-In_2O_3,[54] Pd-SnO_2,[55] Pt-SnO_2,[56] PANI/SnO_2,[57] and Au−SnO_2-CNT;[58] see details in Table S2). (d) Response concentration log−log plots of TiO_2, Pd NPs-TiO_2, and Pd_1-TiO_2 to different concentrations of CO. (e) Responses of Pd_1-TiO_2 sensors to different 100 ppm gases. (f) Column charts of response−recovery times to 100 ppm CO of pristine TiO_2, Pd NPs-TiO_2, and Pd_1-TiO_2 nanoflowers.

X-ray absorption fine structure (XAFS) spectroscopy (see experimental details in SI) was also conducted to further determine the Pd species in Pd_1-TiO_2. The normalized μ(E) spectra of Pd_1-TiO_2 showed higher energy than that of Pd foil, revealing that the Pd species of Pd_1-TiO_2 was in the oxidized state as PdO (Figure 2a). Differed from the Pd foil (a Pd−Pd coordination of 2.79 Å), the Fourier transform of χ(k) of Pd_1-TiO_2 exhibited only one prominent peak (scattering path of Pd−O bonding at 1.84 Å as PdO, Figure 2b). Additionally, such a quantitative χ(R) space (mean Pd−O bonding length of 1.89 Å, Figure 2c and Table S1) and $\chi(k)$ spectra (Figure S8) fittings further evidenced the atomically dispersed Pd atoms in Pd_1-TiO_2. There was only one intensity maximum located at [χ(k), $\chi(R)$] of [4.4, 1.86] (scattering path of Pd−O bonding, Figure 2d) from the Wavelet transform (WT) of χ(k). This result was similar to the feature of PdO ([5.0, 1.74], Figure 2e) but distinct from that of the Pd foil ([9.4, 2.62], Figure 2f). The above results indicate that the local structure was described as follows: each Pd atom on the surface was well coordinated with four O atoms on average (the coordination number of the path Pd−O is 4.3, Table S1; two of them coming from H_2O and EG; another two coming from O atoms shared with Ti atoms, the inset of Figure 2c). Thus, the local structure of the Pd−O−Ti interface, which resembled the highly catalytic SACs, was constructed.

Sensing Performance. Sensing performances of Pd_1-TiO_2 toward CO and its interferences were evaluated in a homemade instrument system developed in our early work.[45] All tests were conducted at (25 ± 1) °C. The responses (R) of Pd_1-TiO_2 to the analytes were determined by detecting the changes in resistance and defined as R (%) = $(r_{gas}/r_{air} - 1) \times 100$ for reducing gases or R (%) = $(r_{air}/r_{gas} - 1) \times 100$ for oxidizing gases (where r_{air} and r_{gas} are the resistance of Pd_1-TiO_2 in air and target gas, respectively). The response and recovery times for Pd_1-TiO_2 were acquired as the times taken to achieve 90% of the total resistance change.

Figure 3a displays the dynamic response−recovery curve of Pd_1-TiO_2 to a broad range of CO (0.1−100 ppm) at RT. The resistance of Pd_1-TiO_2 distinctly increases when exposed to CO and recovers to the initial value when purged with dry air, indicating its good reversibility (Figures 3a and S9a). The average responses (R_{avg}) of five individually fabricated devices toward 100 ppm CO are up to (12 549 ± 494)% (Figures 3b and S10). Comparatively, loaded with only 0.14 at % Pd (data acquired from the XPS test), Pd_1-TiO_2 shows a response 300 times higher than that of the pristine TiO_2 toward 100 ppm CO. However, on loading Pd in the NP form, Pd NPs-TiO_2 (0.16 at % from XPS data) shows a 30 times lower response than that of Pd_1-TiO_2 (Figures 3b and S9 and Table S2). Notably, the response value of Pd_1-TiO_2 to 100 ppm CO at RT is the highest one among all of the reported materials operating at RT, including MO-, low-dimensional material-, polymer-, and molecular sieve-based CO sensors (Figure 3c and Table S2).[9,46] This value is also comparable to those of the best materials working at high temperature (Figure S11 and Table S2). Reproducible and repeatable Pd_1-TiO_2 sensors (Figures 3a and S12a,b) always display significantly higher responses compared to pristine TiO_2 nanoflowers (Figure S12d,e) and Pd NPs-TiO_2 sensors (Figure S12g,h) under the whole measured concentration range (Figures 3d and S12). The linear fitting of the plot deduces the limit of detection (LOD) of Pd_1-TiO_2 as low as 24 ppb by setting the response to 10% (Figure 3d). Notably, this LOD value is 1 order of magnitude lower than the best CO sensor, including the ones obtained at high working temperatures (Figure S13 and Table S2).

SAC sensing materials not only have higher sensitivity according to the above results but also are expected with excellent selectivity.[47,48] To prove it, the sensitivity of Pd_1-TiO_2 to 12 kinds of 100 ppm typical interference analytes was evaluated. As shown in Figure 3e, Pd_1-TiO_2 exhibited responses lower than 20% toward 12 kinds of 100 ppm interference analytes. All of the selectivity coefficients ($S = R_{CO}/R_{gas}$) of Pd_1-TiO_2 between CO and these interference analytes were higher than 630, demonstrating its excellent selectivity. Comparatively, TiO_2 and Pd NPs-TiO_2 showed S values ranging from 1.0 to 6.4 and 7.3 to 44.4, respectively (Figure S14), which reveals the moderate level. Additionally, the responses to the relative humidity (RH) of the above three sensors were also evaluated (Figure S15). The measurements were tested under a lower bias (1 V) to avoid water ionization. On the TiO_2 sensor, the response to 100% RH was more than

https://dx.doi.org/10.1021/acssensors.0c02369
ACS Sens. 2021, 6, 1103−1110

5 orders of magnitude, while on Pd NPs-TiO_2 and Pd_1-TiO_2 sensors, the responses to 100% RH were about more than 4 orders of magnitude. Therefore, all of the samples should be tested under dry air to exclude the effect of water.

The cycling test of Pd_1-TiO_2 sensors toward 10 ppm CO (Figure 3a) was performed to show a low coefficient of variation (CV = 4.42%), which suggests its good repeatability. Meanwhile, the response and recovery times of Pd_1-TiO_2 toward 100 ppm CO are (28 ± 3) and (70 ± 4) s, respectively (Figures 3f and S9a and Table S2). Compared with pristine TiO_2 nanoflowers and Pd NPs-TiO_2, the response of the Pd_1-TiO_2 sensor was speeded up by 600 and 260%, respectively (Figures 3f and S9 and Table S2). These results suggest the fast response−recovery dynamics of Pd_1-TiO_2, which may originate from the rapid adsorption−diffusion−desorption of gas molecules on the surface of Pd_1-TiO_2. Pd_1-TiO_2 also shows good long-term stability. As illustrated in Figure S16, no obvious decay was observed in the CO sensing response of Pd_1-TiO_2 during the test.

Sensing Mechanism. The exact CO sensing mechanism of Pd_1-TiO_2 remains unclear. However, the comparison of the sensing performances among TiO_2, Pd NPs-TiO_2, and Pd_1-TiO_2 elucidates the key role of atomically dispersed Pd atoms played in the high sensing performances. Based on the analysis of the UV−vis spectrum and UPS (see Figures S17 and S18 in the SI), TiO_2, Pd NPs-TiO_2, and Pd_1-TiO_2 displayed the P-type nature. Similar to the cases in other reported P-type sensing materials, oxygen molecules adsorbed on the surface of these materials extract electrons from them and form active oxygen species (e.g., O_2^-) (Figure 4a). This process increases

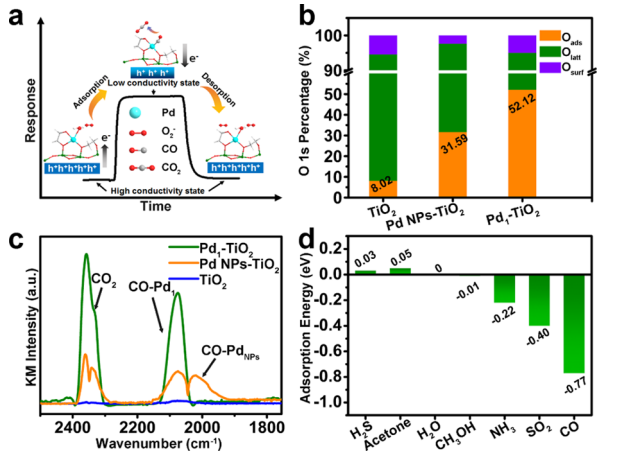

Figure 4. (a) Proposed CO sensing mechanism of Pd_1-TiO_2. (b) Relative percentages of O species from O 1s spectra of TiO_2 nanoflowers, Pd NPs-TiO_2, and Pd_1-TiO_2. (c) DRIFT spectra of TiO_2 nanoflowers, Pd NPs-TiO_2, and Pd_1-TiO_2. (d) Calculated adsorption energies of selected gases on Pd_1-TiO_2.

the hole density in P-type materials and thus results in their high conductivity state (Figure 3a). When exposed to reductive analytes, such as CO, a sensing reaction of the oxidation of the analyte by active oxygen species occurs. The free electrons released from the reaction inject into P-type materials and deplete their hole carriers (Figure 4a), which results in their low conductivity state. After gaseous products left, oxygen molecules adsorb onto sensing materials again and recover their high conductivity state.

As mentioned above, active oxygen species are the reactants for the sensing reaction, whose concentration on the surface of sensing materials significantly affects their sensitivity.[9] XPS measurements reveal that the O 1s envelopes of TiO_2, Pd NPs-TiO_2, and Pd_1-TiO_2 were deconvoluted and assigned to three major subpeaks. They are the lattice oxygen (O_{latt}, 530.2 eV), the adsorbed active oxygen species (O_{ads}, 531.4 eV, mainly O_2^- at RT), and the surface OH group (O_{surf}, 532.6 eV), respectively (Figure S7c). The relative percentages of O_{latt}, O_{ads}, and O_{surf} are illustrated in Figure 4b and Table S3. Comparatively, the pristine TiO_2 has O_{ads} of 8.02%, which increases to 31.59% by Pd loading in Pd NPs-TiO_2. Notably, with comparable Pd loading in the atomic ratio compared to that in Pd NPs-TiO_2 (0.16 at %) but in an atomically dispersed form, Pd_1-TiO_2 (0.14 at %) shows much higher efficiency in increasing O_{ads} with a value as high as 52.12%, which is further confirmed by ESR spectroscopy (Figure S19).

To uncover more details, in situ DRIFT spectroscopy measurements were performed by exposing samples to CO/O_2 (Figures 4c and S20). The adsorption peaks in the ranges of 1900−2200 and 2250−2400 cm^{-1} are assigned to the stretching vibrations of CO and CO_2, respectively. After the same exposing period, the adsorption intensity of CO among the studied materials is in a sequence of TiO_2 < Pd NPs-TiO_2 < Pd_1-TiO_2, indicating that their CO adsorption ability is in the order TiO_2 < Pd NPs-TiO_2 < Pd_1-TiO_2. Accompanying by CO adsorption, CO_2 production (2250−2400 cm^{-1}) is observed on both Pd NPs-TiO_2 and Pd_1-TiO_2 at RT. Under the same time period, the adsorption intensity of CO_2 production on Pd_1-TiO_2 is higher than those on both pristine TiO_2 and Pd NPs-TiO_2, revealing the higher efficiency of Pd_1-TiO_2 on RT CO oxidation for higher sensitivity.

Moreover, DFT theoretical calculations (see details in SI) were carried out to obtain insights into gas selectivity. The calculated energy for the Pd_1-TiO_2 structural model with the coordination of H_2O (Figure S21) was set as a reference. The adsorption energies of analyte molecules were estimated by comparing the energy difference to that of H_2O adsorption. The lower adsorption energy suggests stronger adsorption. The adsorption energy of CO on Pd_1-TiO_2 is calculated to be −0.77 eV (Figure 4d), which is the lowest value compared with those of the interference gases, such as H_2S, acetone, CH_3OH, NH_3, and SO_2. This low adsorption energy may account for the high selectivity of Pd_1-TiO_2 toward CO.

CONCLUSIONS

In summary, we proposed that single-atom catalysts can be used to break through the limits of the sensitivity and selectivity of chemiresistive sensing materials in RT operation. This hypothesis was demonstrated for the first time by employing well-coordinated single Pd atom-based TiO_2 nanoflowers to detect colorless, odorless, and toxic CO at RT. Compared with Pd nanoparticles, Pd SACs drastically enhanced the sensing performances of TiO_2 at RT. As a consequence, Pd_1-TiO_2 possesses: (1) extremely high sensitivity, which is the highest one in all reported sensing materials for RT operation and even comparable to those of the best materials working at high temperature; (2) 1 order of magnitude lower LOD than the best CO sensing materials; (3) very excellent selectivity toward CO among 12 kinds of commonly existing interference gases; (4) remarkably accelerated response and recovery compared with TiO_2 and Pd NPs-TiO_2. The experimental results and theoretical

https://dx.doi.org/10.1021/acssensors.0c02369
ACS Sens. 2021, 6, 1103−1110

calculations revealed the critical roles of atomically dispersed Pd in remarkably increasing the amount of surface-adsorbed O_2^- reagents and constructing a highly catalytic and selective Ti−O−Pd interface via surface coordination for CO oxidation, which results in the ultrahigh sensitivity and selectivity of the sensing material. Since there is a big library of SACs, this work may open a general way to design a new generation of sensing materials and devices, which are in urgent need for constructing environment detection of IoT.

■ ASSOCIATED CONTENT

Supporting Information

The Supporting Information is available free of charge at https://pubs.acs.org/doi/10.1021/acssensors.0c02369.

Morphology characterization of sensors used in this work and selectivity and long-time tests of Pd_1-TiO_2 sensors; humidity evaluation of the sensor; energy band diagrams of the samples; optimized structures of Pd_1-TiO_2-adsorbed gas molecules; and gas sensing properties toward CO of various chemiresistor gas sensors (PDF)

■ AUTHOR INFORMATION

Corresponding Authors

Jiang-Wei Zhang − *Dalian National Laboratory for Clean Energy & State Key Laboratory of Catalysis, Dalian Institute of Chemical Physics, Chinese Academy of Sciences (CAS), Dalian, Liaoning 116023, P. R. China;* orcid.org/0000-0002-1221-3033; Email: jwzhang@dicp.ac.cn

Gang Xu − *State Key Laboratory of Structural Chemistry, Fujian Institute of Research on the Structure of Matter, Chinese Academy of Sciences (CAS), Fuzhou, Fujian 350002, P. R. China; University of Chinese Academy of Sciences, Beijing 100049, P. R. China;* orcid.org/0000-0001-8562-0724; Email: gxu@fjirsm.ac.cn

Authors

Xiao-Liang Ye − *State Key Laboratory of Structural Chemistry, Fujian Institute of Research on the Structure of Matter, Chinese Academy of Sciences (CAS), Fuzhou, Fujian 350002, P. R. China*

Shu-Juan Lin − *State Key Laboratory of Structural Chemistry, Fujian Institute of Research on the Structure of Matter, Chinese Academy of Sciences (CAS), Fuzhou, Fujian 350002, P. R. China*

Hui-Jie Jiang − *State Key Laboratory of Structural Chemistry, Fujian Institute of Research on the Structure of Matter, Chinese Academy of Sciences (CAS), Fuzhou, Fujian 350002, P. R. China*

Lin-An Cao − *State Key Laboratory of Structural Chemistry, Fujian Institute of Research on the Structure of Matter, Chinese Academy of Sciences (CAS), Fuzhou, Fujian 350002, P. R. China*

Ying-Yi Wen − *State Key Laboratory of Structural Chemistry, Fujian Institute of Research on the Structure of Matter, Chinese Academy of Sciences (CAS), Fuzhou, Fujian 350002, P. R. China; University of Chinese Academy of Sciences, Beijing 100049, P. R. China*

Ming-Shui Yao − *State Key Laboratory of Structural Chemistry, Fujian Institute of Research on the Structure of Matter, Chinese Academy of Sciences (CAS), Fuzhou, Fujian 350002, P. R. China*

Wen-Hua Li − *State Key Laboratory of Structural Chemistry, Fujian Institute of Research on the Structure of Matter, Chinese Academy of Sciences (CAS), Fuzhou, Fujian 350002, P. R. China*

Guan-E Wang − *State Key Laboratory of Structural Chemistry, Fujian Institute of Research on the Structure of Matter, Chinese Academy of Sciences (CAS), Fuzhou, Fujian 350002, P. R. China; University of Chinese Academy of Sciences, Beijing 100049, P. R. China*

Complete contact information is available at: https://pubs.acs.org/10.1021/acssensors.0c02369

Author Contributions

G.X. conceived the idea and designed the experiments. X.-L.Y. did the sample synthesis, characterization, and device sensing measurements. H.-J.J. and Y.-Y.W. fabricated the device. L.-A.C. and M.-S.Y. helped to discuss the sensing mechanism. J.-W.Z. performed the XAS tests and discussed the results. G.X., J.-W.Z., X.-L.Y., W.-H.L., and G.-E.W. analyzed the data. G.X., J.-W.Z., and X.-L.Y. wrote the manuscript. S.-J.L. performed the DFT calculations. The manuscript was written through contributions of all authors. All authors have given approval to the final version of the manuscript.

Notes

The authors declare no competing financial interest.

■ ACKNOWLEDGMENTS

This work was supported by the National Natural Science Foundation of China (21822109, 21905280, 2020000052, and 21975254), the Strategic Priority Research Program of CAS (XDB20000000), the International Partnership Program of CAS (121835KYSB201800), the China Postdoctoral Science Foundation (2019M662254), and the Youth Innovation Promotion Association CAS.

■ REFERENCES

(1) WHO, *7 million deaths annually linked to air pollution*; 2016.

(2) OECD, *The Economic Consequences of Outdoor Air Pollution*. Paris, 2016.

(3) Zhao, Q.; Li, X.; Zhou, Q.; Wang, D.; Xu, H. Nanomaterials Developed for Removing Air Pollutants. In *Advanced Nanomaterials for Pollutant Sensing and Environmental Catalysis*; Elsevier, 2020; pp 203−247.

(4) de Gouw, J.; Warneke, C. Measurements of volatile organic compounds in the earth's atmosphere using proton-transfer-reaction mass spectrometry. *Mass. Spectrom. Rev.* **2007**, *26*, 223−257.

(5) Garg, A.; Akbar, M.; Vejerano, E.; Narayanan, S.; Nazhandali, L.; Marr, L. C.; Agah, M. Zebra GC: A mini gas chromatography system for trace-level determination of hazardous air pollutants. *Sens. Actuators, B* **2015**, *212*, 145−154.

(6) Neri, G. First Fifty Years of Chemoresistive Gas Sensors. *Chemosensors* **2015**, *3*, 1−20.

(7) Lee, E.; Yoon, Y. S.; Kim, D.-J. Two-Dimensional Transition Metal Dichalcogenides and Metal Oxide Hybrids for Gas Sensing. *ACS Sens.* **2018**, *3*, 2045−2060.

(8) Li, Z.; Li, H.; Wu, Z.; Wang, M.; Luo, J.; Torun, H.; Hu, P.; Yang, C.; Grundmann, M.; Liu, X.; Fu, Y. Advances in designs and mechanisms of semiconducting metal oxide nanostructures for high-precision gas sensors operated at room temperature. *Mater. Horiz.* **2019**, *6*, 470−506.

(9) Zhang, J.; Liu, X.; Neri, G.; Pinna, N. Nanostructured Materials for Room-Temperature Gas Sensors. *Adv. Mater.* **2016**, *28*, 795−831.

(10) Ji, H.; Zeng, W.; Li, Y. Gas sensing mechanisms of metal oxide semiconductors: a focus review. *Nanoscale* **2019**, *11*, 22664−22684.

(11) Xiong, W.; Ndokoye, P.; Leung, M. K. Noble Metal−Based Nanosensors for Environmental Detection. In *Advanced Nanomaterials for Pollutant Sensing and Environmental Catalysis*; Elsevier, 2020; pp 39−78.
(12) Chen, X.; Liu, L.; Huang, F. Black titanium dioxide (TiO_2) nanomaterials. *Chem. Soc. Rev.* **2015**, *44*, 1861−1885.
(13) Zhang, Q.; Kusada, K.; Wu, D.; Yamamoto, T.; Toriyama, T.; Matsumura, S.; Kawaguchi, S.; Kubota, Y.; Kitagawa, H. Selective control of fcc and hcp crystal structures in Au−Ru solid-solution alloy nanoparticles. *Nat. Commun.* **2018**, *9*, No. 510.
(14) Liu, P.; Zhao, Y.; Qin, R.; Gu, L.; Zhang, P.; Fu, G.; Zheng, N. A vicinal effect for promoting catalysis of Pd1/TiO_2: supports of atomically dispersed catalysts play more roles than simply serving as ligands. *Sci. Bull.* **2018**, *63*, 675−682.
(15) Kim, D.; Xie, C.; Becknell, N.; Yu, Y.; Karamad, M.; Chan, K.; Crumlin, E. J.; Nørskov, J. K.; Yang, P. Electrochemical Activation of CO_2 through Atomic Ordering Transformations of AuCu Nanoparticles. *J. Am. Chem. Soc.* **2017**, *139*, 8329−8336.
(16) Bai, J.; Li, Y.; Liu, Y.; Wang, H.; Liu, F.; Liu, F.; Sun, P.; Yan, X.; Lu, G. $Au_{39}Rh_{61}$ Alloy Nanocrystal-Decorated $W_{18}O_{49}$ for Enhanced Detection of n-Butanol. *ACS Sens.* **2019**, *4*, 2662−2670.
(17) Qiao, B.; Wang, A.; Yang, X.; Allard, L. F.; Jiang, Z.; Cui, Y.; Liu, J.; Li, J.; Zhang, T. Single-atom catalysis of CO oxidation using Pt1/FeOx. *Nat. Chem.* **2011**, *3*, 634−641.
(18) Ji, S.; Chen, Y.; Wang, X.; Zhang, Z.; Wang, D.; Li, Y. Chemical Synthesis of Single Atomic Site Catalysts. *Chem. Rev.* **2020**, *120*, 11900−11955.
(19) Li, Z.; Ji, S.; Liu, Y.; Cao, X.; Tian, S.; Chen, Y.; Niu, Z.; Li, Y. Well-Defined Materials for Heterogeneous Catalysis: From Nanoparticles to Isolated Single-Atom Sites. *Chem. Rev.* **2020**, *120*, 623−682.
(20) Zhang, H.; Liu, G.; Shi, L.; Ye, J. Single-Atom Catalysts: Emerging Multifunctional Materials in Heterogeneous Catalysis. *Adv. Energy Mater.* **2018**, *8*, No. 1701343.
(21) Jiao, L.; Jiang, H.-L. Metal-Organic-Framework-Based Single-Atom Catalysts for Energy Applications. *Chem* **2019**, *5*, 786−804.
(22) Lee, B.-H.; Park, S.; Kim, M.; Sinha, A. K.; Lee, S. C.; Jung, E.; Chang, W. J.; Lee, K.-S.; Kim, J. H.; Cho, S.-P.; Kim, H.; Nam, K. T.; Hyeon, T. Reversible and cooperative photoactivation of single-atom Cu/TiO_2 photocatalysts. *Nat. Mater.* **2019**, *18*, 620−626.
(23) Yan, H.; Su, C.; He, J.; Chen, W. Single-atom catalysts and their applications in organic chemistry. *J. Mater. Chem. A* **2018**, *6*, 8793−8814.
(24) Liu, P.; Zhao, Y.; Qin, R.; Mo, S.; Chen, G.; Gu, L.; Chevrier, D. M.; Zhang, P.; Guo, Q.; Zang, D.; Wu, B.; Fu, G.; Zheng, N. Photochemical route for synthesizing atomically dispersed palladium catalysts. *Science* **2016**, *352*, 797−800.
(25) Qiao, B.; Liu, J.; Wang, Y.-G.; Lin, Q.; Liu, X.; Wang, A.; Li, J.; Zhang, T.; Liu, J. Highly Efficient Catalysis of Preferential Oxidation of CO in H_2-Rich Stream by Gold Single-Atom Catalysts. *ACS Catal.* **2015**, *5*, 6249−6254.
(26) Xie, P.; Pu, T.; Nie, A.; Hwang, S.; Purdy, S. C.; Yu, W.; Su, D.; Miller, J. T.; Wang, C. Nanoceria-Supported Single-Atom Platinum Catalysts for Direct Methane Conversion. *ACS Catal.* **2018**, *8*, 4044−4048.
(27) Wan, J.; Chen, W.; Jia, C.; Zheng, L.; Dong, J.; Zheng, X.; Wang, Y.; Yan, W.; Chen, C.; Peng, Q.; Wang, D.; Li, Y. Defect Effects on TiO_2 Nanosheets: Stabilizing Single Atomic Site Au and Promoting Catalytic Properties. *Adv. Mater.* **2018**, *30*, No. 1705369.
(28) Tian, S.; Gong, W.; Chen, W.; Lin, N.; Zhu, Y.; Feng, Q.; Xu, Q.; Fu, Q.; Chen, C.; Luo, J.; Yan, W.; Zhao, H.; Wang, D.; Li, Y. Regulating the Catalytic Performance of Single-Atomic-Site Ir Catalyst for Biomass Conversion by Metal−Support Interactions. *ACS Catal.* **2019**, *9*, 5223−5230.
(29) Jiang, Z.; Feng, X.; Deng, J.; He, C.; Douthwaite, M.; Yu, Y.; Liu, J.; Hao, Z.; Zhao, Z. Atomic-Scale Insights into the Low-Temperature Oxidation of Methanol over a Single-Atom Pt1-Co_3O_4 Catalyst. *Adv. Funct. Mater.* **2019**, *29*, No. 1902041.
(30) Lin, L.; Yao, S.; Gao, R.; Liang, X.; Yu, Q.; Deng, Y.; Liu, J.; Peng, M.; Jiang, Z.; Li, S.; Li, Y.-W.; Wen, X.-D.; Zhou, W.; Ma, D. A highly CO-tolerant atomically dispersed Pt catalyst for chemoselective hydrogenation. *Nat. Nanotechnol.* **2019**, *14*, 354−361.
(31) Pei, G. X.; Liu, X. Y.; Wang, A.; Lee, A. F.; Isaacs, M. A.; Li, L.; Pan, X.; Yang, X.; Wang, X.; Tai, Z.; Wilson, K.; Zhang, T. Ag Alloyed Pd Single-Atom Catalysts for Efficient Selective Hydrogenation of Acetylene to Ethylene in Excess Ethylene. *ACS Catal.* **2015**, *5*, 3717−3725.
(32) Marcinkowski, M. D.; Yuk, S. F.; Doudin, N.; Smith, R. S.; Nguyen, M.-T.; Kay, B. D.; Glezakou, V.-A.; Rousseau, R.; Dohnálek, Z. Low-Temperature Oxidation of Methanol to Formaldehyde on a Model Single-Atom Catalyst: Pd Atoms on Fe_3O_4(001). *ACS Catal.* **2019**, *9*, 10977−10982.
(33) Lang, R.; Xi, W.; Liu, J.-C.; Cui, Y.-T.; Li, T.; Lee, A. F.; Chen, F.; Chen, Y.; Li, L.; Li, L.; Lin, J.; Miao, S.; Liu, X.; Wang, A.-Q.; Wang, X.; Luo, J.; Qiao, B.; Li, J.; Zhang, T. Non defect-stabilized thermally stable single-atom catalyst. *Nat. Commun.* **2019**, *10*, No. 234.
(34) Guan, H.; Lin, J.; Qiao, B.; Miao, S.; Wang, A.-Q.; Wang, X.; Zhang, T. Enhanced performance of Rh1/TiO_2 catalyst without methanation in water-gas shift reaction. *AIChE J.* **2017**, *63*, 2081−2088.
(35) Tang, Y.; Asokan, C.; Xu, M.; Graham, G. W.; Pan, X.; Christopher, P.; Li, J.; Sautet, P. Rh single atoms on TiO_2 dynamically respond to reaction conditions by adapting their site. *Nat. Commun.* **2019**, *10*, No. 4488.
(36) Gu, F.; Cui, Y.; Han, D.; Hong, S.; Flytzani-Stephanopoulos, M.; Wang, Z. Atomically dispersed Pt (II) on WO_3 for highly selective sensing and catalytic oxidation of triethylamine. *Appl. Catal., B* **2019**, *256*, No. 117809.
(37) Koga, K. Electronic and Catalytic Effects of Single-Atom Pd Additives on the Hydrogen Sensing Properties of Co_3O_4 Nanoparticle Films. *ACS Appl. Mater. Interfaces* **2020**, *12*, 20806−20823.
(38) Xu, Y.; Zheng, W.; Liu, X.; Zhang, L.; Zheng, L.; Yang, C.; Pinna, N.; Zhang, J. Platinum single atoms on tin oxide ultrathin films for extremely sensitive gas detection. *Mater. Horiz.* **2020**, *7*, 1519−1527.
(39) Sun, L.; Wang, B.; Wang, Y. High-Temperature Gas Sensor Based on Novel Pt Single Atoms@SnO_2 Nanorods@SiC Nanosheets Multi-heterojunctions. *ACS Appl. Mater. Interfaces* **2020**, *12*, 21808−21817.
(40) Gu, F.; Di, M.; Han, D.; Hong, S.; Wang, Z. Atomically Dispersed Au on In_2O_3 Nanosheets for Highly Sensitive and Selective Detection of Formaldehyde. *ACS Sens.* **2020**, *5*, 2611−2619.
(41) Cao, L.; Liu, W.; Luo, Q.; Yin, R.; Wang, B.; Weissenrieder, J.; Soldemo, M.; Yan, H.; Lin, Y.; Sun, Z.; Ma, C.; Zhang, W.; Chen, S.; Wang, H.; Guan, Q.; Yao, T.; Wei, S.; Yang, J.; Lu, J. Atomically dispersed iron hydroxide anchored on Pt for preferential oxidation of CO in H_2. *Nature* **2019**, *565*, 631−635.
(42) Xiang, G.; Li, T.; Zhuang, J.; Wang, X. Large-scale synthesis of metastable TiO_2(B) nanosheets with atomic thickness and their photocatalytic properties. *Chem. Commun.* **2010**, *46*, 6801−6803.
(43) Yao, M.-S.; Tang, W.-X.; Wang, G.-E.; Nath, B.; Xu, G. MOF Thin Film-Coated Metal Oxide Nanowire Array: Significantly Improved Chemiresistor Sensor Performance. *Adv. Mater.* **2016**, *28*, 5229−5234.
(44) Ge, X.; Zhou, P.; Zhang, Q.; Xia, Z.; Chen, S.; Gao, P.; Zhang, Z.; Gu, L.; Guo, S. Palladium Single Atoms on TiO_2 as a Photocatalytic Sensing Platform for Analyzing the Organophosphorus Pesticide Chlorpyrifos. *Angew. Chem., Int. Ed.* **2020**, *59*, 232−236.
(45) Yao, M.-S.; Lv, X.-J.; Fu, Z.-H.; Li, W.-H.; Deng, W.-H.; Wu, G.-D.; Xu, G. Layer-by-Layer Assembled Conductive Metal−Organic Framework Nanofilms for Room-Temperature Chemiresistive Sensing. *Angew. Chem., Int. Ed.* **2017**, *56*, 16510−16514.
(46) Mahajan, S.; Jagtap, S. Metal-oxide semiconductors for carbon monoxide (CO) gas sensing: A review. *Appl. Mater. Today* **2020**, *18*, No. 100483.

https://dx.doi.org/10.1021/acssensors.0c02369
ACS Sens. 2021, 6, 1103−1110

(47) Peterson, E. J.; DeLaRiva, A. T.; Lin, S.; Johnson, R. S.; Guo, H.; Miller, J. T.; Hun Kwak, J.; Peden, C. H. F.; Kiefer, B.; Allard, L. F.; Ribeiro, F. H.; Datye, A. K. Low-temperature carbon monoxide oxidation catalysed by regenerable atomically dispersed palladium on alumina. *Nat. Commun.* **2014**, *5*, No. 4885.
(48) Mehdi, D. E.; Soheila, A. Exploring different reaction mechanisms for oxidation of CO over a single Pd atom incorporated nitrogen-doped graphene: A DFT study. In *Applied Surface Science*; Elsevier, 2018; Vol. *463*, pp 526−534.
(49) Su, J.; Zou, X.-X.; Zou, Y.-C.; Li, G.-D.; Wang, P.-P.; Chen, J.-S. Porous Titania with Heavily Self-Doped Ti^{3+} for Specific Sensing of CO at Room Temperature. *Inorg. Chem.* **2013**, *52*, 5924−5930.
(50) Wang, L.; Chai, R.; Lou, Z.; Shen, G. Highly sensitive hybrid nanofiber-based room-temperature CO sensors: Experiments and density functional theory simulations. *Nano Res.* **2018**, *11*, 1029−1037.
(51) Su, P.-G.; Chen, F.-Y.; Wei, C.-H. Simple one-pot polyol synthesis of Pd nanoparticles, TiO_2 microrods and reduced graphene oxide ternary composite for sensing NH_3 gas at room temperature. *Sens. Actuators, B* **2018**, *254*, 1125−1132.
(52) Choi, S.-W.; Kim, S. S. Room temperature CO sensing of selectively grown networked ZnO nanowires by Pd nanodot functionalization. *Sens. Actuators, B* **2012**, *168*, 8−13.
(53) Lai, H.-Y.; Chen, C.-H. Highly sensitive room-temperature CO gas sensors: Pt and Pd nanoparticle-decorated In_2O_3 flower-like nanobundles. *J. Mater. Chem.* **2012**, *22*, 13204−13208.
(54) Fu, H.; Hou, C.; Gu, F.; Han, D.; Wang, Z. Facile preparation of rod-like Au/In_2O_3 nanocomposites exhibiting high response to CO at room temperature. *Sens. Actuators, B* **2017**, *243*, 516−524.
(55) Marikutsa, A. V.; Rumyantseva, M. N.; Yashina, L. V.; Gaskov, A. M. Role of surface hydroxyl groups in promoting room temperature CO sensing by Pd-modified nanocrystalline SnO_2. *J. Solid State Chem.* **2010**, *183*, 2389−2399.
(56) Wang, K.; Zhao, T.; Lian, G.; Yu, Q.; Luan, C.; Wang, Q.; Cui, D. Room temperature CO sensor fabricated from Pt-loaded SnO_2 porous nanosolid. *Sens. Actuators, B* **2013**, *184*, 33−39.
(57) Jian, K.-S.; Chang, C.-J.; Wu, J. J.; Chang, Y.-C.; Tsay, C.-Y.; Chen, J.-H.; Horng, T.-L.; Lee, G.-J.; Karuppasamy, L.; Anandan, S.; Chen, C.-Y. High Response CO Sensor Based on a Polyaniline/SnO_2 Nanocomposite. *Polymers* **2019**, *11*, 184.
(58) Du, N.; Zhang, H.; Ma, X.; Yang, D. Homogeneous coating of Au and SnO_2 nanocrystals on carbon nanotubesvialayer-by-layer assembly: a new ternary hybrid for a room-temperature CO gas sensor. *Chem. Commun.* **2008**, *345*, 6182−6184.

https://dx.doi.org/10.1021/acssensors.0c02369
ACS Sens. 2021, 6, 1103−1110